ACS OMEGA

http://pubs.acs.org/journal/acsodf

Article

Semiconducting Chalcogenide Alloys Based on the (Ge, Sn, Pb) (S, Se, Te) Formula with Outstanding Properties: A First-Principles Calculation Study

Asadollah Bafekry,* Masoud Shahrokhi, Aamir Shafique, Hamad R. Jappor, Mohamed M. Fadlallah, Catherine Stampfl, Mitra Ghergherehchi,* Muhammad Mushtaq, Seyed Amir Hossein Feghhi, and Daniela Gogova

Cite This: *ACS Omega* 2021, 6, 9433−9441

Read Online

ACCESS | Metrics & More | Article Recommendations | Supporting Information

ABSTRACT: Very recently, a new class of the multicationic and -anionic entropy-stabilized chalcogenide alloys based on the (Ge, Sn, Pb) (S, Se, Te) formula has been successfully fabricated and characterized experimentally [Zihao Deng *et al., Chem. Mater. 32,* 6070 (**2020**)]. Motivated by the recent experiment, herein, we perform density functional theory-based first-principles calculations in order to investigate the structural, mechanical, electronic, optical, and thermoelectric properties. The calculations of the cohesive energy and elasticity parameters indicate that the alloy is stable. Also, the mechanical study shows that the alloy has a brittle nature. The GeSnPbSSeTe alloy is a semiconductor with a direct band gap of 0.4 eV (0.3 eV using spin−orbit coupling effect). The optical analysis illustrates that the first peak of Im(ε) for the GeSnPbSSeTe alloy along all polarization directions is located in the visible range of the spectrum which renders it a promising material for applications in optical and electronic devices. Interestingly, we find an optically anisotropic character of this system which is highly desirable for the design of polarization-sensitive photodetectors. We have accurately predicted the thermoelectric coefficients and have calculated a large power factor value of 3.7×10^{11} W m^{-1} K^{-2} s^{-1} for p-type. The high p-type power factor is originated from the multiple valleys near the valence band maxima. The anisotropic results of the optical and transport properties are related to the specific tetragonal alloy unit cell.

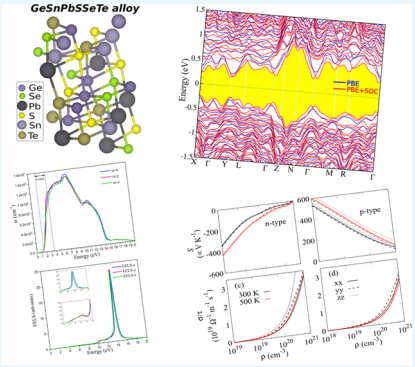

INTRODUCTION

The IV−VI compounds have aroused considerable recent attention due to their extraordinary properties such as anharmonic effects,[1] weak lattice thermal conductivity,[2,3] unprecedented thermoelectric performance,[4−7] complex band structure,[8] chemical ultrahigh power factor,[9] chemical stability, and a lesser degree of toxicity.[10] Some of these compounds display ferroelectricity, paraelectricity, and superconductivity.[11−13] In addition, most IV−VI compounds have a band gap size[14] that makes them suitable for devices such as infrared detectors and lasers, nanoelectronics, and thermoelectrics.[15,16] Semiconductor chalcogenides are a special class of IV−VI compound materials that contain at least one element of the following: tellurium (Te), selenium (Se), sulphur (S), or polonium (Po). Due to their optoelectronic, microelectronic, and high thermoelectric performance, chalcogenide compounds have now become an intense area of scientific research.[17−21] Currently, chalcogenides are very interesting for applications in all industrial sectors.[22] So far, SnS,[23,24] SnTe,[25,26] SnSe,[27−29] GeSe,[30,31] GeTe,[32−34] PbS,[35−37] PbTe,[38−40] and PbSe[41,42] are among the most studied category of IV−VI semiconductor chalcogenides. However, progressive advancements are anticipated once it is possible to obtain materials with any required characteristics which can be adapted to particular applications. These materials will also enable many new applications but not all properties are obtainable directly by the fabricated elemental or binary materials.[43] Therefore, the most widespread and easiest method to tune the properties is by making an alloy of two or more different elements.

From this standpoint, several groups have experimentally examined the alloying consequences of IV−VI compounds and attained materials with preferable properties. Specifically, Hu and co-workers[44] investigated the impact of the alloying element number on the electrical transport characteristic and lattice thermal conductivity in SnTe, (Sn, Ge)Te, (Ge, Sn, Pb, Mn), (Ge, Sn, Pb, Mn)Te, and (Ge, Sn, Pb)Te. Their results

Received: December 11, 2020
Accepted: March 18, 2021
Published: March 30, 2021

attest that the alloying enhances the power factors, the band effective mass, and the character of the band. Furthermore, Qin *et al.*[45] reported a thorough investigation of p-type PbTe−PbSe−PbS alloys and the results indicate that the alloying plays an important role in the enhancement of the Seebeck coefficient, power factor, and electrical conductivity and reduction of the thermal conductivity. Likewise, remarkable thermal efficiency has been observed in alloys of SnSe−SnS,[46] PbSe−PbS,[47] PbTe−PbS,[48] PbTe−PbSe,[49] and $SnS_{1-x}Se_x$.[50] Moreover, high thermoelectric performance has been attained in the following systems, $Ge_xPb_{1-x}Te$,[51,52] $GeTe_{1-x}Se_x$,[53] PbSnTeSe,[54] (Pb,Sn,Ge)Te,[55] $Pb_{1-x}Sn_xTe$-PbS,[56] $Ge_{1-x}Pb_xTe$,[5,51] and $(GeTe)_{1-2x}(GeSe)_x(GeS)_x$.[57] With regard to optoelectronic properties, the alloying of semiconductors brings about an increase in carrier mobility and an apparent change in the optical properties.[58−60] To illustrate, Tan *et al.*[61] carried out a methodical study of the optoelectronic properties of Se_xTe_{1-x} alloys by the thermal evaporation method. Their results revealed that Se_xTe_{1-x} alloys are promising materials for the manufacture of infrared photodetectors. Most importantly, very recently, the GeSnPbSSeTe alloys were fabricated and experimentally prepared by alloying six elements (Ge, Sn, Pb, S, Se, and Te).[62] The experimental and theoretical results demonstrated that the obtained chalcogenide alloys are kinetically metastable at ambient temperatures and stable at the temperature of growth. Furthermore, electronic transport measurements confirm that the fabricated high-entropy materials are semiconductors, which can therefore make these chalcogenide alloys promising for functional applications such as in photovoltaics, thermoelectric devices, and optoelectronics. To the best of our knowledge, there have been no theoretical studies that report the physical properties of this newly synthesized alloy (GeSnPbSSeTe). However, the aforementioned study that focuses on the thermoelectric properties inspires us to thoroughly investigate the unexplored properties of (Ge, Sn, Pb) (S, Se, Te) chalcogenide alloys. We also report some optoelectronic properties of chalcogenide alloys built on the (Ge, Sn, Pb) (S, Se, Te) formula.

In the present work, we investigate the electronic, structural, thermodynamic, and optical properties of (Ge, Sn, Pb) (S, Se, Te) alloys using density functional theory (DFT). Our studies reveal that this alloy, GeSnPbSSeTe, is a stable semiconductor with a direct band gap. In addition, the obtained physical properties may stimulate scientists and engineers to develop and produce new types of optoelectronic and nanoelectronic devices. We also wish to emphasize that the comparison of our model results with experimental data can only be for a large supercell size since the latter strongly depends on the method of preparation and size of the alloy due to many structure configuration probabilities.

RESULTS AND DISCUSSION

Structure Properties. The atomic structure of the alloy and its super cell, for different views, is illustrated in Figure 1a. The GeSnPbSSeTe alloy crystal structure has the space group P_1 and is composed of 36 atoms (involving 6 Ge, 6 Sn, 6 Pb, 6 S, 6 Se, and 6 Te atoms). After structure optimization, the size of the alloy in the *x*-, *y*-, and *z*-direction is found to be 11.34, 9.69, and 12.34 Å, respectively. The perspective view of the optimized atomic structure, with structural parameters such as bond length and bond angles, is shown in Figure 1b. The calculated Pb−S and Pb−Te bond lengths are 2.81 and 3.17 Å, respectively, while the bond lengths of Ge−Te and Ge−Sn are

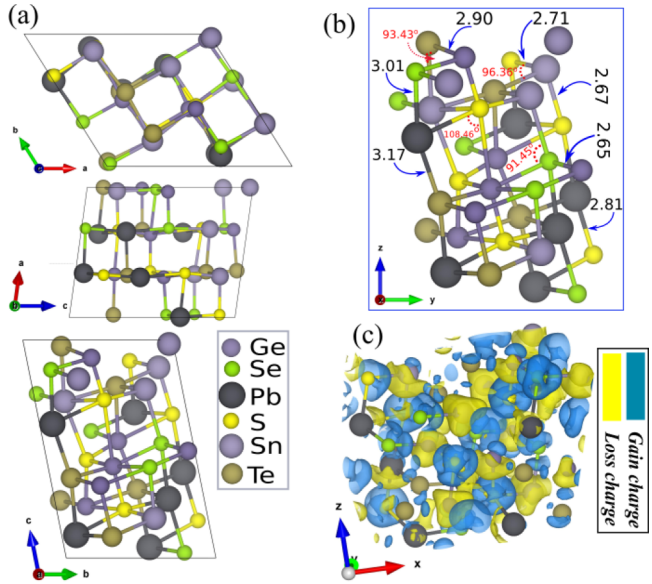

Figure 1. (a) Different view of the atomic structure, (b) optimized structure with structural parameters, and (c) difference charge density of the GeSnPbSSeTe alloy.

2.90 and 2.65 Å, respectively. We can see that they increase as the atomic radius increases. The difference charge density of the GeSnPbSSeTe alloy is shown in Figure 1c. The charge accumulation and depletion are indicated by color, with blue and yellow regions, respectively. The results show that the positively charged Ge, Sn, and Pb atoms are surrounded by negatively charged S, Se, and Te atoms. Based on the Bader charge-transfer analysis, we find that the S, Se, and Te atoms gain 0.95*e*, 0.83*e*, and 0.55*e* from the adjacent Ge, Sn, and Pb atoms (see Table 1). According to the Pauling electronegativity scale, S (2.5), Se (2.4), and Te (2.1) atoms have a larger electronegativity than Ge (1.8), Sn (1.8), and Pb (1.9) which results in the significant difference in the electron density.

The cohesive energy E_{coh} is given by $E_{coh} = E_{tot} - 6(E_{Ge} + E_{Sn} + E_{Pb} + E_S + E_{Se} + E_{Te})/n_{tot}$, where E_{Ge}, E_{Sn}, E_{Pb}, E_S, E_{Se}, E_{Te}, and E_{tot} represent the energies of isolated Ge, Sn, Pb, S, Se, and Te atoms and total energy of the alloy, respectively, and n_{tot} is the total number of atoms. The cohesive energy is found to be −3.36 eV/atom. The negative energy indicates that the formation of the structure is exothermic.

The work function, $\Phi = E_{vacuum} - E_F$, for the (100) alloy surface is calculated using the electrostatic potential of the alloy and where E_{vacuum} is the energy of vacuum which is a planar and E_F is the Fermi energy. We find that Φ = 4.6 eV w is higher than the corresponding value of Sn (4.2 eV[82]), Pb (4.1 eV[82]), Sn−Pb alloy (3.6−4.2 eV[82]), and In−Sn alloy (4.0−4.4 eV[82]) and less than the work functions of Te (4.9 eV[83]), Se (5.9 eV[83]), and Ge (5.0 eV[83]).

Mechanical Properties. For mechanical properties such as elastic constants, we used the stress−strain relationship based on Hooke's law to evaluate the elasticity: $\delta_{ij} = C_{ij}\epsilon_{ij}$, where δ_{ij}, C_{ij}, and ϵ_{ij} indicate the stress, elastic stiffness, and strain tensors, respectively (see the Supporting Information). Table 2 includes the values of elastic constants of the (Ge, Sn, Pb) (S, Se, Te) alloy which is mechanically stable.[77] All the diagonal components have large values as compared to the other components. The elastic constants are used to calculate other

https://doi.org/10.1021/acsomega.0c06024
ACS Omega 2021, 6, 9433−9441

Table 1. Structural and Electronic Parameters for the Optimized GeSnPbSSeTe Alloy Shown in Figure 1b Including the Size of the Supercell in the *x*-, *y*-, and *z*-Direction *x*, *y* and *z*, the Bond Angles between the *x*-, *y*-, and *z*-Direction *x* and *y* (α), *x* and *z* (β), and *y* and *z* (γ), the Bond Lengths between Ge−Te (d_1), Ge−Sn (d_2), Pb−S (d_3), and Pb−Te (d_4), the Cohesive Energy Per Atom, (E_{coh}); the Charge Transfer to S (ΔQ_1), Se (ΔQ_2), and Te (ΔQ_3) Atoms; the Work Function (Φ); the Band Gap (E_g) of PBE (HSE06) is Shown Outside (Inside) Parentheses, the VBM and CBM Positions, and the Young's Modulus (C) and Poisson's Ratio (ν) are Shown Outside and Inside Parentheses, Respectively

sys.	*a* (Å)	*b* (Å)	*c* (Å)	$d_{1,2}$ (Å)	$d_{3,4}$ (Å)	α (deg)	β (deg)	γ (deg)	E_{coh} (eV/atom)	$\Delta Q_{1,2,3}$ (e)	Φ (eV)	E_g (eV)	VBM/CBM	$C(\nu)$ GPa (−)
alloy	11.34	9.69	12.34	2.90, 2.65	2.81, 3.17	108.73	73.21	125.01	−3.36	0.95, 0.83, 0.55		0.4 (0.9)	Y/Y	40.2 (0.21)

Table 2. Elastic Constants of the GeSnPbSSeTe Alloy

C_{11}	C_{12}	C_{13}	C_{14}	C_{15}	C_{16}
58.0	20.3	8.5	5.5	0.7	−8.32
C_{22}	C_{23}	C_{24}	C_{25}	C_{26}	C_{33}
33.1	6.1	−4.0	2.0	−4.4	53.05
C_{34}	C_{35}	C_{36}	C_{44}	C_{45}	C_{46}
−2.5	−8.4	4.7	21.9	−3.1	−2.3
C_{55}		C_{56}		C_{66}	
11.5		−2.3		12.6	

elastic parameters, for example, bulk modulus (B), shear modulus (G), and Young's modulus using Voigt−Reuss−Hill approximation.[78] In the Voigt regime, we find that the Young's modulus is 40.21 GPa, and the Poisson's ratio is 0.22 which means that the GeSnPbSSeTe alloy has a brittle behavior (it is less than 0.33[79]). Also, we find that the bulk modulus (B) is 23.72 GPa which measures the ability of the alloy to resist compressing under applied external force. The shear modulus (B) is 16.48 GPa which represents the resistance of the shape change of the alloy, where G increases as the rigidity of the alloy increases. The B/G ratio describes the ductile or brittle nature of the alloy, which is an important factor in mechanical applications. We find that the ratio is 1.44 which indicates that the GeSnPbSSeTe alloy has a brittle nature because it is less than 1.75.[80]

Electronic and Optical Properties. Regarding the electronic properties, the band structure of the GeSnPbSSeTe alloy, Figure 2, shows a semiconducting behavior with a direct

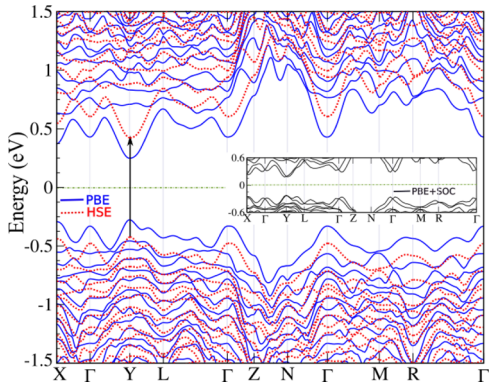

Figure 2. Electronic band structure of the GeSnPbSSeTe alloy within PBE and HSE06 functionals. The band structure with PBE + SOC indicated as the inset. The Fermi level is set to zero.

band gap of 0.4 eV, at the Y symmetry point within the PBE functional. Inclusion of spin−orbit coupling (SOC) decreases the band gap to 0.3 eV with degenerate states as compared to the PBE result. The corresponding density of states (DOS) and projected DOS (PDOS) show that the p states of Ge, Sn, and Pb are dominant in the conduction band, such as p_x and p_z while the s, p_x, and p_z states of Se and Te are dominant at the top of the valence band. The S, Se, and Te states are dominant below −1 eV (see Figure 3). The inset figure shows that the Pb states have more contribution at the bottom of the conduction band, while Te and S states have minor contributions. On the other hand, the Te states have large contributions in the valence band, while Pb states have less contribution. The band gap increases to 0.9 eV when the hybrid exchange−correlation functional HSE06 is used. We can claim that the semiconducting direct band gap of the alloy is preserved within the

https://doi.org/10.1021/acsomega.0c06024
ACS Omega 2021, 6, 9433−9441

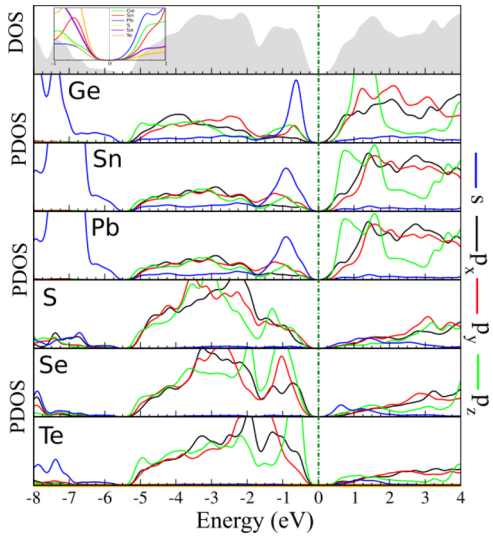

Figure 3. DOS and PDOS of the GeSnPbSSeTe alloy. The Fermi level is set to zero.

HSE functional. Only the edges of the valence band and conduction bands are shifted to lower and higher energy, respectively, as compared to the corresponding edges determined by the PBE calculation.

Next, we discuss the optical response of this novel crystal structure using the RPA method constructed over the HSE06 approach. The imaginary and real parts of the dielectric function are illustrated in Figure 2a. Our results show that the dielectric function of this compound becomes anisotropic along the *x*-, *y*-, and *z*-directions. The anisotropic behavior of the dielectric constants can be attributed to the tetragonal structure of the alloy. The Im(ε) is the sum of all transitions from the valence bands (VBs) to the conduction bands (CBs).

The first maximum of Im(ε) for this structure is located at the energy 2.87, 2.82, and 2.29 eV along *x*-, *y*-, and *z*-directions, respectively, which is in the visible range of light. The static dielectric constants (real part of the dielectric constant at zero energy) for this compound are calculated to be 15.57, 14.62, and 14.97 for $E\|x$, $E\|y$, and $E\|z$, respectively. In the Drude model, the plasma frequencies are defined by the roots of Re(ε) with the $x = 0$ line[72−74] and are calculated for this system. The corresponding values of the first plasma frequencies along *x*-, *y*-, and *z*-axes are at 3.06, 3.26, and 3.38 eV, respectively. Another root of Re(ε) with the $x = 0$ line for this system occurs at an energy of ∼14 eV which is related to the main plasma frequencies related to electron energy loss spectra. The absorption coefficient, α, for this compound along all polarizations is also plotted in Figure 4b. The absorption edge of this structure occurs at an energy of 1.10 eV that is

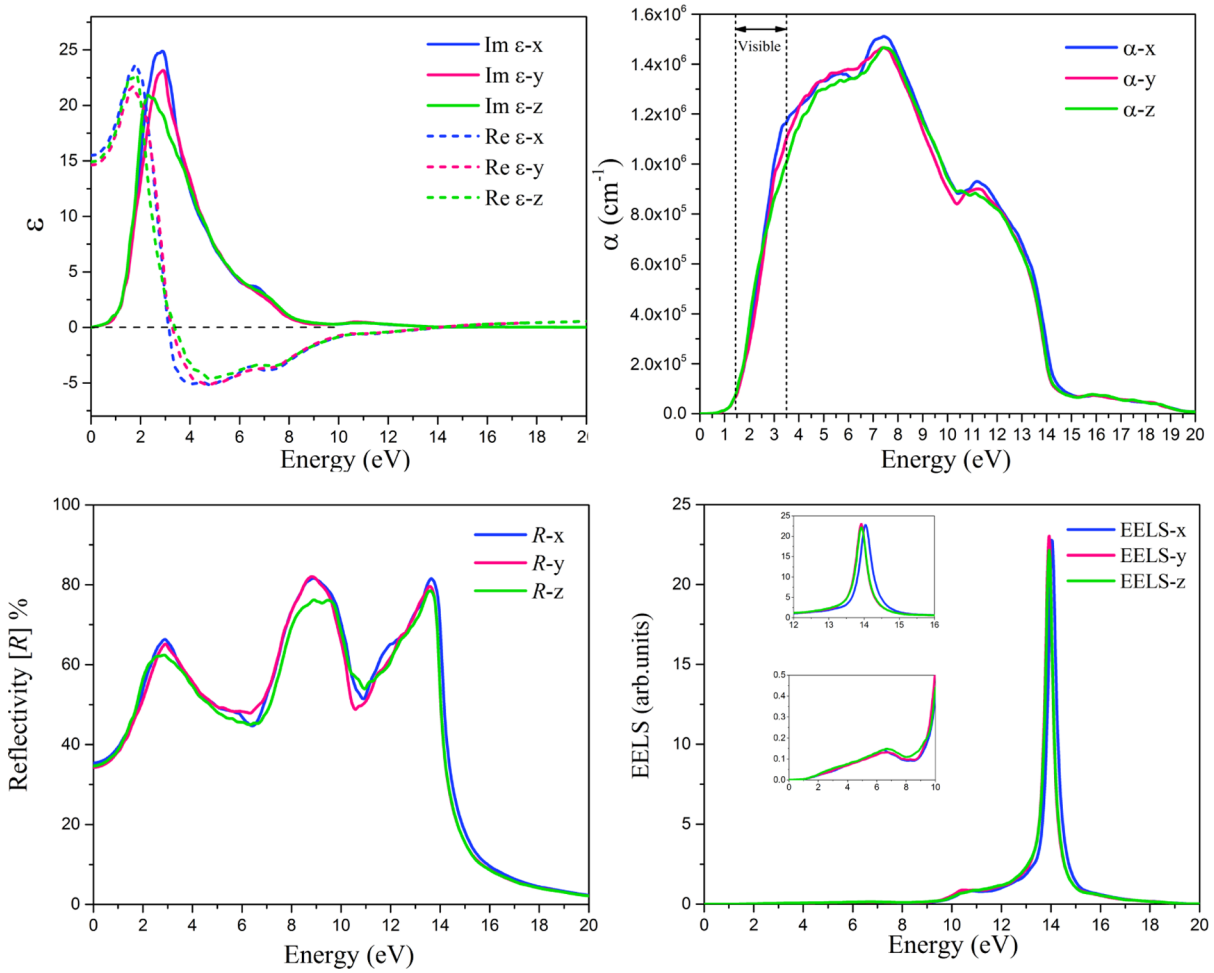

Figure 4. Imaginary and real parts of the (a) dielectric function, (b) absorption coefficient, (c) reflectivity, and (d) electron energy loss spectra as a function of photon energy for the GeSnPbSSeTe alloy, as predicted using the random-phase approximation (RPA) + HSE06 approach.

https://doi.org/10.1021/acsomega.0c06024
ACS Omega 2021, 6, 9433−9441

related to the optical transition from p-states of the VB of Te atoms to the p-states of the CB of Pb atoms. It is evident that this material possesses a strong absorption in the visible region of light ($\sim 10^5$ cm^{-1}) which is higher than the typical absorption coefficient values of direct band gap semiconductors across the entire visible range.[75] The main peak of the absorption spectrum along all directions occurs around 7.44 eV, which exhibits significant UV absorption for this compound.

The reflectivity for the GeSnPbSSeTe bulk system for all directions of the electric field is shown in Figure 4c. Our results show that the reflectivity at E = 0 eV is ∼35% resulting in semiconductor behavior. Furthermore, the reflectivity for this system in the energy range between 8−10 and 12−14 eV is a maximum, while transmission is less in this energy range. For photon energy greater than 15 eV, the reflectivity is the lowest along all directions where the transmission reaches its maximum. In the next step, we discuss the electron energy loss spectraof GeSnPbSSeTe, as depicted in Figure 4d. The electron energy loss spectroscopy EELS technique is useful in revealing plasma resonance phenomena as distinct from normal interband transitions.[76] It is known that the sharp peaks in the energy-loss function are associated with plasma oscillations and consistent with the roots of Re(ε) with the x = 0 line. It is obvious that the GeSnPbSSeTe bulk system has one main peak in the EELS spectra which is associated with the plasma oscillations. The highest peak values in Figure 4d for $E\|x$, $E\|y$, and $E\|z$ are obtained at 14.05, 13.95, and 13.90 eV for the plasmon energy. It is clear that at these energies, the Re(ε) goes through zero (Figure 4a).

Thermoelectric Properties. The excellent features of the band structure, such as multivalleys, direct band gap, *and so forth*, of this alloy material prompted us to calculate its thermoelectric coefficients: the Seebeck coefficient (S), electrical conductivity (σ/τ), electronic thermal conductivity (κ^e/τ), and power factor ($S^2\sigma/\tau$) along x-, y-, and z-directions as a function of carrier concentration at 300 and 500 K are shown in Figure 5. S increases for increasing temperature, while it decreases for increasing carrier concentration, as shown in Figure 5a,b. The $|S|$ is proportional to $N_v^{3/2}m^*$, where N_v is the number of the degenerate band valleys and m^* is the carrier effective mass.[81] Therefore, due to the presence of multivalleys near the valence band maxima, the S for the p-type doping is higher than that for n-type doping. Next, we investigate the σ/τ and κ^e/τ, both these quantities increase with respect to carrier concentration and we find that they are significantly larger for the n-type doping at the same carrier concentration. Additionally, the σ/τ and κ^e/τ for the both n-type and p-type decrease with respect to temperature at fixed carrier concentration because the carrier scattering rate increases as temperature increases. A high power factor (PF) plays an important role in achieving high thermoelectric efficiency and Figure 5g,h illustrates the calculated PF as a function of carrier concentration. The PF for the p-type material is almost double that of the n-type due to the intrinsic degeneracy of valence valleys, which shows that the p-type thermoelectric properties are dominant in this material. The optimal PF values are 3.27 and 1.62 (10^{11} W m^{-1} K^{-2} s^{-1}) for p-type doping at 500 and 300 K, respectively. We also find significant anisotropy in the PF with $PF_z/PF_x \sim 1.64$ for p-type doping and $PF_z/PF_x \sim 2.33$ for n-type doping at 500 K (due to the specific tetragonal unit cell). The higher PF indicates that this material can be promising for thermoelectric applications.

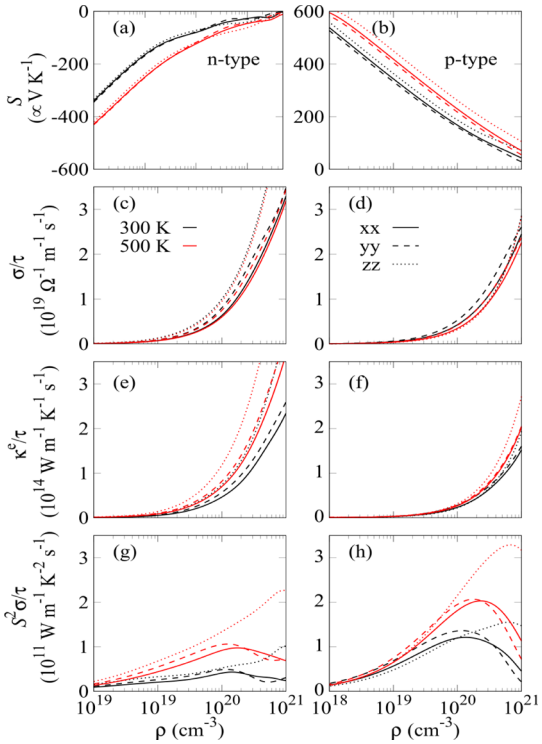

Figure 5. Electronic transport properties of GeSnPbSSeTe as a function of carrier concentration for n-type-doped (left side) and p-type-doped (right side) at 300 and 500 K. (a,b) Seebeck coefficient S, (c,d) scaled electrical conductivity σ/τ, (e,f) scaled electronic thermal conductivity κ^e/τ, and (g,h) power factor $S^2\sigma/\tau$.

CONCLUSIONS

The density functional theory is employed to discuss the structural, mechanical, electronic, optical, and thermoelectric properties of a recently synthesized GeSnPbSSeTe alloy. Notice that the cohesive energy calculations and elasticity parameters indicate that the alloy is stable. We found that the alloy is a direct semiconductor with a 0.4 eV band gap, while with the SOC, the band gap decreased to 0.3 eV. The dominant states at the top of the valence band are Se and Te while at the bottom of the conduction band are Ge, Sn, and Pb. The linear photon energy-dependent optical response of the GeSnPbSSeTe bulk system, including the imaginary and real part of dielectric function, absorption coefficient, reflectivity, and electron energy loss spectra for all polarizations, was investigated at the RPA + HSE06 level. Our results show that this material possesses strong absorption in the visible region of light, suggesting its potential for applications in optoelectronics, photovoltaics, and nanoelectronics. The multiple valleys around the valence band maxima give rise to a high thermopower S, which leads to a very high p-type PF, for example, even reaching 3.27×10^{11} W m^{-1} K^{-2} s^{-1} at 500 K within the BTE transport mechanism.

COMPUTATIONAL METHODS

The structural optimization and electronic properties were performed using the plane-wave basis projector augmented wave (PAW) method in the framework of DFT. The generalized gradient approximation (GGA) with the Perdew−Burke−Ernzerhof (PBE)[63,64] functional was used for the exchange−correlation functional as implemented in the Vienna *Ab initio* Simulation Package (VASP).[65,66] Moreover, for the

https://doi.org/10.1021/acsomega.0c06024
ACS Omega 2021, 6, 9433−9441

band structure calculations, spin−orbit coupling (SOC) was included on top of GGA. Furthermore the hybrid functional HSE06[67] with the mixing parameter of 0.25 and a screening parameter of 0.2 was used to calculate the band structure of the alloy. Analysis of the charge transfer in the structures was carried out using the Bader technique.[68] The kinetic energy cutoff for the plane-wave expansion was set to 500 eV and the energy was minimized until its variation in the following steps became 10^{-8} eV. To obtain optimized structures, the total Hellmann−Feynman forces were reduced to 10^{-7} eV/Å. A 21 × 21 × 21 Γ-centered *k*-point sampling was used for the supercell using the Monkhorst−Pack scheme.[69] The optical calculations were performed in the RPA[70] method constructed over the screened hybrid HSE06 functional using VASP. The optical calculations, such as the imaginary and real parts of the dielectric tensor (Im(ε) and Re(ε)), absorption coefficient (α), reflectivity (R), and EELS spectra, were performed in the RPA[70] method constructed over the screened hybrid Heyd−Scuseria−Ernzerhof functional (HSE06).[67] The convergence criterion for the electronic self-consistent loop was set to 10−6 eV. The optical and mechanical properties were evaluated using a dense *k*-point grid of 8 × 8 × 8 Γ-centered Monkhorst−Pack.[69] More details on the calculation of the optical and mechanical properties can be found in the Supporting Information. The electronic transport coefficients are obtained using the Boltzmann transport equation under constant relaxation time approximations together with rigid band approximation as implemented in the Boltztrap2 code.[71]

The electronic transport coefficients are calculated from the following equations

$$S^{\alpha\beta}(T,\mu) = \frac{1}{eT\Omega\sigma^{\alpha\beta}(T,\mu)}\int\sigma^{\alpha\beta}(\varepsilon)(\varepsilon-\mu)\left[-\frac{\partial f_0(T,\varepsilon,\mu)}{\partial\varepsilon}\right]d\varepsilon \quad (1)$$

$$\sigma^{\alpha\beta}(T,\mu) = \frac{1}{\Omega}\int\sigma^{\alpha\beta}(\varepsilon)\left[-\frac{\partial f_0(T,\varepsilon,\mu)}{\partial\varepsilon}\right]d\varepsilon \quad (2)$$

$$\kappa_e^{\alpha\beta}(T,\mu) = \frac{1}{e^2T\Omega}\int\sigma^{\alpha\beta}(\varepsilon)(\varepsilon-\mu)^2\left[-\frac{\partial f_0(T,\varepsilon,\mu)}{\partial\varepsilon}\right]d\varepsilon \quad (3)$$

where T, f_0, μ, and $\Xi(\epsilon)$ represent the temperature, Fermi-Dirac distribution function, chemical potential, and transport distribution function, respectively. $\Xi(\epsilon)$ is obtained using the following equation

$$\Xi^{\alpha,\beta}(\varepsilon) = \sum_{\vec{k}}\delta(\varepsilon-\varepsilon_k)(\vec{k})v_k^\alpha v_k^\beta\tau_k$$

where v_k^α is the group velocity of the αth component with wave vector k, τ_k is the relaxation time with wave vector k, and ϵ is the energy of holes and electrons. For accurate calculation of the electronic transport coefficients, we used a dense *k*-point mesh of 16 × 16 × 16.

■ ASSOCIATED CONTENT

Supporting Information

The Supporting Information is available free of charge at https://pubs.acs.org/doi/10.1021/acsomega.0c06024.

Computational details for the optical and mechanical calculations (PDF)

■ AUTHOR INFORMATION

Corresponding Authors

Asadollah Bafekry − *Department of Radiation Application, Shahid Beheshti University, 19839 69411 Tehran, Iran; Department of Physics, University of Antwerp, B-2020 Antwerp, Belgium;* orcid.org/0000-0002-9297-7382; Email: bafekry.asad@gmail.com

Mitra Ghergherehchi − *College of Electronic and Electrical Engineering, Sungkyunkwan University, 440-746 Suwon, Korea*; Email: mitragh@skku.edu

Authors

Masoud Shahrokhi − *Department of Physics, Faculty of Science, University of Kurdistan, 66177-15175 Sanandaj, Iran;* orcid.org/0000-0003-3656-6551

Aamir Shafique − *Department of Physics, Lahore University of Management Sciences, 54792 Lahore, Pakistan*

Hamad R. Jappor − *Department of Physics, College of Education for Pure Sciences, University of Babylon, 964 Hilla, Iraq;* orcid.org/0000-0002-8885-3985

Mohamed M. Fadlallah − *Department of Physics, Faculty of Science, Benha University, 13518 Benha, Egypt*

Catherine Stampfl − *School of Physics, The University of Sydney, New South Wales 2006, Australia*

Muhammad Mushtaq − *Department of Physics, Women University of Azad Jammu and Kashmir, 12500 Bagh, Pakistan*

Seyed Amir Hossein Feghhi − *Department of Radiation Application, Shahid Beheshti University, 19839 69411 Tehran, Iran*

Daniela Gogova − *Department of Physics, University of Oslo, 0316 Oslo, Norway*

Complete contact information is available at: https://pubs.acs.org/10.1021/acsomega.0c06024

Notes

The authors declare no competing financial interest.

■ ACKNOWLEDGMENTS

This work was supported by the National Research Foundation of Korea (NRF) grant funded by the Korea government (MSIT) (NRF-2015M2B2A4033123). Also, this work is funded by the Research Council of Norway (RCN) SALIENT project (239895/F20).

■ REFERENCES

(1) Delaire, O.; Ma, J.; Marty, K.; May, A. F.; McGuire, M. A.; Du, M.-H.; Singh, D. J.; Podlesnyak, A.; Ehlers, G.; Lumsden, M. D.; Sales, B. C. Giant anharmonic phonon scattering in PbTe. *Nat. Mater.* **2011**, *10*, 614−619.

(2) Wang, H.; Gibbs, Z. M.; Takagiwa, Y.; Snyder, G. J. Tuning bands of PbSe for better thermoelectric efficiency. *Energy Environ. Sci.* **2014**, *7*, 804−811.

(3) Pei, Y.; Shi, X.; Lalonde, A.; Wang, H.; Chen, L.; Snyder, G. J. Convergence of electronic bands for high performance bulk thermoelectrics. *Nat* **2011**, *473*, 66−69.

(4) Wang, H.; Pei, Y.; Lalonde, A. D.; Snyder, G. J. Heavily doped p-type PbSe with high thermoelectric performance: An alternative for PbTe. *Adv. Mater.* **2011**, *23*, 1366−1370.

(5) Wu, D.; Zhao, L. D.; Hao, S.; Jiang, Q.; Zheng, F.; Doak, J. W.; Wu, H.; Chi, H.; Gelbstein, Y.; Uher, C.; Wolverton, C.; Kanatzidis,

M.; He, J. Origin of the high performance in GeTe-based thermoelectric materials upon Bi_2Te_3 doping. *J. Am. Chem. Soc.* **2014**, *136*, 11412−11419.
(6) Pei, Y.; Lalonde, A. D.; Wang, H.; Snyder, G. J. Low effective mass leading to high thermoelectric performance. *Energy Environ. Sci.* **2012**, *5*, 7963−7969.
(7) Chen, C.-L.; Wang, H.; Chen, Y.-Y.; Day, T.; Snyder, G. J. Thermoelectric properties of p-type polycrystalline SnSe doped with Ag. *J. Mater. Chem. A.* **2014**, *2*, 11171−11176.
(8) Cagnoni, M.; Führen, D.; Wuttig, M. Thermoelectric Performance of IV-VI Compounds with Octahedral-Like Coordination: A Chemical-Bonding Perspective. *Adv. Mater.* **2018**, *30*, 1801787.
(9) Zhao, L.-D.; Tan, G.; Hao, S.; He, J.; Pei, Y.; Chi, H.; Wang, H.; Gong, S.; Xu, H.; Dravid, V. P.; Uher, C.; Snyder, G. J.; Wolverton, C.; Kanatzidis, M. G. Ultrahigh power factor and thermoelectric performance in hole-doped single-crystal SnSe. *Sci* **2016**, *351*, 141−144.
(10) Qin, G.; Qin, Z.; Fang, W.-Z.; Zhang, L.-C.; Yue, S.-Y.; Yan, Q.-B.; Hu, M.; Su, G. Diverse anisotropy of phonon transport in two-dimensional group IV-VI compounds: A comparative study. *Nanoscale* **2016**, *8*, 11306−11319.
(11) Ronneberger, I.; Zanolli, Z.; Wuttig, M.; Mazzarello, R. Changes of Structure and Bonding with Thickness in Chalcogenide Thin Films. *Adv. Mater.* **2020**, *32*, 2001033.
(12) Gui, X.; Górnicka, K.; Chen, Q.; Zhou, H.; Klimczuk, T.; Xie, W. Superconductivity in Metal-Rich Chalcogenide Ta2Se. *Inorg. Chem.* **2020**, *59*, 5798−5802.
(13) Zhang, J.-J.; Guan, J.; Dong, S.; Yakobson, B. I. Room-Temperature Ferroelectricity in Group-IV Metal Chalcogenide Nanowires. *J. Am. Chem. Soc.* **2019**, *141*, 15040−15045.
(14) Cohen, M. L.; Chelikowsky, J. R. *Electronic Structure and Optical Properties of Semiconductors*; Springer: Berlin, Heidelberg, 1988.
(15) Ding, G.; Gao, G.; Yao, K. High-efficient thermoelectric materials: The case of orthorhombic IV-VI compounds. *Sci. Rep.* **2015**, *5*, 9567.
(16) Patel, M.; Kim, H.-S.; Kim, J. Wafer-scale production of vertical SnS multilayers for high-performing photoelectric devices. *Nanoscale* **2017**, *9*, 15804−15812.
(17) Qiu, Y.; Jin, Y.; Wang, D.; Guan, M.; He, W.; Peng, S.; Liu, R.; Gao, X.; Zhao, L.-D. Realizing high thermoelectric performance in GeTe through decreasing the phase transition temperature via entropy engineering. *J. Mater. Chem. A* **2019**, *7*, 26393−26401.
(18) Shafique, A.; Shin, Y. H. Thermoelectric and phonon transport properties of two-dimensional IV-VI compounds. *Sci. Rep.* **2017**, *7*, 506.
(19) Hodges, J. M.; Hao, S.; Grovogui, J. A.; Zhang, X.; Bailey, T. P.; Li, X.; Gan, Z.; Hu, Y. Y.; Uher, C.; Dravid, V. P.; Wolverton, C.; Kanatzidis, M. G. Chemical Insights into PbSe- x%HgSe: High Power Factor and Improved Thermoelectric Performance by Alloying with Discordant Atoms. *J. Am. Chem. Soc.* **2018**, *140*, 18115−18123.
(20) Zakery, A.; Elliott, S. R. Optical properties and applications of chalcogenide glasses: A review. *J. Non-Cryst. Solids* **2003**, *330*, 1−12.
(21) Hien, N. D.; Cuong, N. Q.; Bui, L. M.; Dinh, P. C.; Nguyen, C. V.; Phuc, H. V.; Hieu, N. V.; Jappor, H. R.; Phuong, L. T. T.; Hoi, B. D.; Nhan, L. C.; Hieu, N. N. First principles study of single-layer SnSe2 under biaxial strain and electric field: Modulation of electronic properties. *Phys. E* **2019**, *111*, 201−205.
(22) Velea, A.; Opsomer, K.; Devulder, W.; Dumortier, J.; Fan, J.; Detavernier, C.; Jurczak, M.; Govoreanu, B. Te-based chalcogenide materials for selector applications. *Sci. Rep.* **2017**, *7*, 8103.
(23) Guo, R.; Wang, X.; Kuang, Y.; Huang, B. First-principles study of anisotropic thermoelectric transport properties of IV-VI semiconductor compounds SnSe and SnS. *Phys. Rev. B: Condens. Matter Mater. Phys.* **2015**, *92*, 115202.
(24) Cheng, C.-H.; Chi, Y.-C.; Wu, C.-L.; Lin, C.-J.; Tsai, L.-H.; Chang, J.-H.; Chen, M. K.; Shih, M.-H.; Lee, C.-K.; Wu, C.-I.; Tsai, D. P.; Lin, G.-R. Catalytically solid-phase self-organization of nanoporous SnS with optical depolarizability. *Nanoscale* **2016**, *8*, 4579−4587.
(25) Tan, X.; Tan, X.; Liu, G.; Xu, J.; Shao, H.; Hu, H.; Jin, M.; Jiang, H.; Jiang, J. Optimizing the thermoelectric performance of In-Cd codoped SnTe by introducing Sn vacancies. *J. Mater. Chem. C* **2017**, *5*, 7504−7509.
(26) Zhou, M.; Gibbs, Z. M.; Wang, H.; Han, Y.; Xin, C.; Li, L.; Snyder, G. J. Optimization of thermoelectric efficiency in SnTe: The case for the light band. *Phys. Chem. Chem. Phys.* **2014**, *16*, 20741−20748.
(27) Zhao, L.-D.; Lo, S.-H.; Zhang, Y.; Sun, H.; Tan, G.; Uher, C.; Wolverton, C.; Dravid, V. P.; Kanatzidis, M. G. Ultralow thermal conductivity and high thermoelectric figure of merit in SnSe crystals. *Nature* **2014**, *508*, 373−377.
(28) Efthimiopoulos, I.; Berg, M.; Bande, A.; Puskar, L.; Ritter, E.; Xu, W.; Marcelli, A.; Ortolani, M.; Harms, M.; Müller, J.; Speziale, S.; Koch-Müller, M.; Liu, Y.; Zhao, L.-D.; Schade, U. Effects of temperature and pressure on the optical and vibrational properties of thermoelectric SnSe. *Phys. Chem. Chem. Phys.* **2019**, *21*, 8663−8678.
(29) Liu, M.; Zhang, J.; Xu, J.; Hu, B.; Sun, K.; Yang, Y.; Wang, J.; Du, B.; Zhang, H. The crystallization, thermodynamic and thermoelectric properties of vast off-stoichiometric Sn-Se crystals. *J. Mater. Chem. C* **2020**, *8*, 6422−6434.
(30) Yuan, K.; Sun, Z.; Zhang, X.; Gong, X.; Tang, D. A first-principles study of the thermoelectric properties of rhombohedral GeSe. *Phys. Chem. Chem. Phys.* **2020**, *22*, 1911−1922.
(31) Chen, B.; Ruan, Y.; Li, J.; Wang, W.; Liu, X.; Cai, H.; Yao, L.; Zhang, J. M.; Chen, S.; Chen, G. Highly oriented GeSe thin film: Self-assembly growth: Via the sandwiching post-annealing treatment and its solar cell performance. *Nanoscale* **2019**, *11*, 3968−3978.
(32) Chen, Y.; Sun, L.; Zhou, Y.; Zewdie, G. M.; Deringer, V. L.; Mazzarello, R.; Zhang, W. Chemical understanding of resistance drift suppression in Ge-Sn-Te phase-change memory materials. *J. Mater. Chem. C* **2019**, *8*, 71−77.
(33) Ren, K.; Zhu, M.; Song, W.; Lv, S.; Xia, M.; Wang, Y.; Lu, Y.; Ji, Z.; Song, Z. Electrical switching properties and structural characteristics of GeSe-GeTe films. *Nanoscale* **2019**, *11*, 1595−1603.
(34) Nam, K.-H.; Sung, G.-K.; Choi, J.-H.; Youn, J.-S.; Jeon, K.-J.; Park, C.-M. New high-energy-density GeTe-based anodes for Li-ion batteries. *J. Mater. Chem. A.* **2019**, *7*, 3278−3288.
(35) Abargues, R.; Navarro, J.; Rodríguez-Cantó, P. J.; Maulu, A.; Sánchez-Royo, J. F.; Martínez-Pastor, J. P. Enhancing the photocatalytic properties of PbS QD solids: The ligand exchange approach. *Nanoscale* **2019**, *11*, 1978−1987.
(36) Hu, L.; Huang, S.; Patterson, R.; Halpert, J. E. Enhanced mobility in PbS quantum dot films via PbSe quantum dot mixing for optoelectronic applications. *J. Mater. Chem. C* **2019**, *7*, 4497−4502.
(37) Ma, C.; Shi, C.; Lv, K.; Ying, C.; Fan, S.; Yang, Y. Gradient-band-gap strategy for efficient solid-state PbS quantum-dot sensitized solar cells. *Nanoscale* **2019**, *11*, 8402−8407.
(38) Heremans, J. P.; Jovovic, V.; Toberer, E. S.; Saramat, A.; Kurosaki, K.; Charoenphakdee, A.; Yamanaka, S.; Snyder, G. J. Enhancement of thermoelectric efficiency in PbTe by distortion of the electronic density of states. *Sci* **2008**, *321*, 554−557.
(39) Rojas-Chávez, H.; Cruz-Martínez, H.; Flores-Rojas, E.; Juárez-García, J. M.; González-Domínguez, J. L.; Daneu, N.; Santoyo-Salazar, J. The mechanochemical synthesis of PbTe nanostructures: Following the Ostwald ripening effect during milling. *Phys. Chem. Chem. Phys.* **2018**, *20*, 27082−27092.
(40) Bafekry, A.; Stampfl, C.; Peeters, F. M. The Electronic, Optical, and Thermoelectric Properties of Monolayer PbTe and the Tunability of the Electronic Structure by External Fields and Defects. *Phys. Status Solidi* **2020**, *257*, 2000182.
(41) Roy, P.; Nguyen, T. P. Ab initio calculation of pentacene-PbSe hybrid interface for photovoltaic applications. *Phys. Chem. Chem. Phys.* **2016**, *18*, 18209−18218.
(42) Han, L.; Liu, J.; Yu, N.; Liu, Z.; Gu, J.; Lu, J.; Ma, W. Facile synthesis of ultra-small PbSe nanorods for photovoltaic application. *Nanoscale* **2015**, *7*, 2461−2470.

https://doi.org/10.1021/acsomega.0c06024
ACS Omega 2021, 6, 9433−9441

(43) Ning, C.-Z.; Dou, L.; Yang, P. Bandgap engineering in semiconductor alloy nanomaterials with widely tunable compositions. *Nat. Rev. Mater.* **2017**, *2*, 17070.
(44) Hu, L.; Zhang, Y.; Wu, H.; Li, J.; Li, Y.; Mckenna, M.; He, J.; Liu, F.; Pennycook, S. J.; Zeng, X. Entropy Engineering of SnTe: Multi-Principal-Element Alloying Leading to Ultralow Lattice Thermal Conductivity and State-of-the-Art Thermoelectric Performance. *Adv. Energy Mater.* **2018**, *8*, 1802116.
(45) Qin, B.; Hu, X.; Zhang, Y.; Wu, H.; Pennycook, S. J.; Zhao, L. D. Comprehensive Investigation on the Thermoelectric Properties of p-Type PbTe-PbSe-PbS Alloys. *Adv. Electron. Mater.* **2019**, *5*, 1900609.
(46) Zhang, Q.; Chere, E. K.; Sun, J.; Cao, F.; Dahal, K.; Chen, S.; Chen, G.; Ren, Z. Studies on Thermoelectric Properties of n-type Polycrystalline SnSe1-xSxby Iodine Doping. *Adv. Energy Mater.* **2015**, *5*, 1500360.
(47) Wang, H.; Wang, J.; Cao, X.; Snyder, G. J. Thermoelectric alloys between PbSe and PbS with effective thermal conductivity reduction and high figure of merit. *J. Mater. Chem. A.* **2014**, *2*, 3169−3174.
(48) Wu, H. J.; Zhao, L.-D.; Zheng, F. S.; Wu, D.; Pei, Y. L.; Tong, X.; Kanatzidis, M. G.; He, J. Q. Broad temperature plateau for thermoelectric figure of merit ZT > 2 in phase-separated $PbTe_0.7S_0.3$. *Nat. Commun.* **2014**, *5*, 4515.
(49) Pei, Y.; Tan, G.; Feng, D.; Zheng, L.; Tan, Q.; Xie, X.; Gong, S.; Chen, Y.; Li, J.-F.; He, J.; Kanatzidis, M. G.; Zhao, L.-D. Integrating Band Structure Engineering with All-Scale Hierarchical Structuring for High Thermoelectric Performance in PbTe System. *Adv. Energy Mater.* **2017**, *7*, 1601450.
(50) He, W.; Wang, D.; Wu, H.; Xiao, Y.; Zhang, Y.; He, D.; Feng, Y.; Hao, Y.-J.; Dong, J.-F.; Chetty, R.; Hao, L.; Chen, D.; Qin, J.; Yang, Q.; Li, X.; Song, J.-M.; Zhu, Y.; Xu, W.; Niu, C.; Li, X.; Wang, G.; Liu, C.; Ohta, M.; Pennycook, S. J.; He, J.; Li, J.-F.; Zhao, L.-D. High thermoelectric performance in low-cost SnS0.91Se0.09 crystals. *Sci* **2019**, *365*, 1418−1424.
(51) Gelbstein, Y.; Davidow, J. Highly efficient functional GexPb1−xTe based thermoelectric alloys. *Phys. Chem. Chem. Phys.* **2014**, *16*, 20120−20126.
(52) Gelbstein, Y.; Davidow, J.; Leshem, E.; Pinshow, O.; Moisa, S. Significant lattice thermal conductivity reduction following phase separation of the highly efficient Ge x Pb1-x Te thermoelectric alloys. *Phys. Status Solidi* **2014**, *251*, 1431−1437.
(53) Li, J.; Zhang, X.; Lin, S.; Chen, Z.; Pei, Y. Realizing the High Thermoelectric Performance of GeTe by Sb-Doping and Se-Alloying. *Chem. Mater.* **2017**, *29*, 605−611.
(54) Fan, Z.; Wang, H.; Wu, Y.; Liu, X.; Lu, Z. Thermoelectric performance of PbSnTeSe high-entropy alloys. *Mater. Res. Lett.* **2017**, *5*, 187−194.
(55) Gelbstein, Y.; Ben-Yehuda, O.; Pinhas, E.; Edrei, T.; Sadia, Y.; Dashevsky, Z.; Dariel, M. P. Thermoelectric properties of (Pb,Sn,Ge)-te-based alloys. *J. Electron. Mater.* **2009**, *38*, 1478−1482.
(56) Androulakis, J.; Lin, C.-H.; Kong, H.-J.; Uher, C.; Wu, C.-I.; Hogan, T.; Cook, B. A.; Caillat, T.; Paraskevopoulos, K. M.; Kanatzidis, M. G. Spinodal Decomposition and Nucleation and Growth as a Means to Bulk Nanostructured Thermoelectrics: Enhanced Performance in Pb1-xSnxTe−PbS. *J. Am. Chem. Soc.* **2007**, *129*, 9780−9788.
(57) Samanta, M.; Biswas, K. Low Thermal Conductivity and High Thermoelectric Performance in (GeTe)1-2x(GeSe)x(GeS)x: Competition between Solid Solution and Phase Separation. *J. Am. Chem. Soc.* **2017**, *139*, 9382−9391.
(58) Aminorroaya Yamini, S.; Patterson, V.; Santos, R. Band-Gap Nonlinearity in Lead Chalcogenide (PbQ, Q = Te, Se, S) Alloys. *ACS Omega* **2017**, *2*, 3417−3423.
(59) Obeid, M. M.; Shukur, M. M.; Edrees, S. J.; Khenata, R.; Ghebouli, M. A.; Khandy, S. A.; Bouhemadou, A.; Jappor, H. R.; Wang, X. Electronic band structure, thermodynamics and optical characteristics of BeO1−A (A = S, Se, Te) alloys: Insights from ab initio study. *Chem. Phys.* **2019**, *526*, 110414.
(60) Obeid, M. M.; Stampfl, C.; Bafekry, A.; Guan, Z.; Jappor, H. R.; Nguyen, C. V.; Naseri, M.; Hoat, D. M.; Hieu, N. N.; Krauklis, A. E.; Vu, T. V.; Gogova, D. First-principles investigation of nonmetal doped single-layer BiOBr as a potential photocatalyst with a low recombination rate. *Phys. Chem. Chem. Phys.* **2020**, *22*, 15354−15364.
(61) Tan, C.; Amani, M.; Zhao, C.; Hettick, M.; Song, X.; Lien, D. H.; Li, H.; Yeh, M.; Shrestha, V. R.; Crozier, K. B.; Scott, M. C.; Javey, A. Evaporated Se x Te 1- x Thin Films with Tunable Bandgaps for Short-Wave Infrared Photodetectors. *Adv. Mater.* **2020**, *32*, 2001329.
(62) Deng, Z.; Olvera, A.; Casamento, J.; Lopez, J. S.; Williams, L.; Lu, R.; Shi, G.; Poudeu, P. F. P.; Kioupakis, E. Semiconducting High-Entropy Chalcogenide Alloys with Ambi-ionic Entropy Stabilization and Ambipolar Doping. *Chem. Mater.* **2020**, *32*, 6070−6077.
(63) Perdew, J. P.; Burke, K.; Ernzerhof, M. Generalized gradient approximation made simple. *Phys. Rev. Lett.* **1996**, *77*, 3865.
(64) Perdew, J. P.; Burke, K.; Ernzerhof, M. Generalized Gradient Approximation Made Simple [Phys. Rev. Lett. 77, 3865 (1996)]. *Phys. Rev. Lett.* **1997**, *78*, 1396.
(65) Kresse, G.; Hafner, J. Ab initiomolecular dynamics for liquid metals. *Phys. Rev. B: Condens. Matter Mater. Phys.* **1993**, *47*, 558.
(66) Kresse, G.; Hafner, J. Ab initiomolecular-dynamics simulation of the liquid-metal-amorphous-semiconductor transition in germanium. *Phys. Rev. B: Condens. Matter Mater. Phys.* **1994**, *49*, 14251.
(67) Heyd, J.; Scuseria, G. E. Efficient Hybrid Density Functional Calculations in Solids: Assessment of the Heyd-Scuseria-Ernzerhof Screened Coulomb Hybrid Functional. *J. Chem. Phys.* **2004**, *121*, 1187−1192.
(68) Henkelman, G.; Arnaldsson, A.; Jónsson, H. A fast and robust algorithm for Bader decomposition of charge density. *Comput. Mater. Sci.* **2006**, *36*, 354.
(69) Monkhorst, H. J.; Pack, J. D. Special points for Brillouin-zone integrations. *Phys. Rev. B: Solid State* **1976**, *13*, 5188.
(70) Gajdoš, M.; Hummer, K.; Kresse, G.; Furthmuller, J.; Bechstedt, F. Linear optical properties in the projector-augmented wave methodology. *Phys. Rev. B: Condens. Matter Mater. Phys.* **2006**, *73*, 045112.
(71) Madsen, G. K. H.; Carrete, J.; Verstraete, M. J. BoltzTraP2, A Program for Interpolating Band Structures and Calculating Semi-Classical Transport Coefficients. *Comput. Phys. Commun.* **2018**, *231*, 140−145.
(72) Wooten, F. *Optical Properties of Solids*; Academic Press, 2013.
(73) Shahrokhi, M.; Naderi, S.; Fathalian, A. Ab initio calculations of optical properties of B2C graphene sheet. *Solid State Commun.* **2012**, *152*, 1012−1017.
(74) Shahrokhi, M.; Leonard, C. Tuning the band gap and optical spectra of silicon-doped graphene: many-body effects and excitonic states. *J. Alloys Compd.* **2017**, *693*, 1185.
(75) Shahrokhi, M.; Raybaud, P.; Le Bahers, T. On the understanding of the optoelectronic properties of S-doped MoO3 and O-doped MoS2 bulk systems: a DFT perspective. *J. Mater. Chem. C* **2020**, *8*, 9064−9074.
(76) Shahrokhi, M.; Leonard, C. Quasi-particle energies and optical excitations of wurtzite BeO and its nanosheet. *J. Alloys Compd.* **2016**, *682*, 254−262.
(77) Mouhat, F.; Coudert, F.-X. Necessary and sufficient elastic stability conditions in various crystal systems. *Phys. Rev. B: Condens. Matter Mater. Phys.* **2014**, *90*, 224104.
(78) Hill, R. The Elastic Behaviour of a Crystalline Aggregate. *Proc. Phys. Soc., London, Sect. A* **1952**, *65*, 349.
(79) Hu, W.-C.; Liu, Y.; Li, D.-J.; Zeng, X.-Q.; Xu, C.-S. First-principles study of structural and electronic properties of C14-type Laves phase Al2Zr and Al2Hf. *Comput. Mater. Sci.* **2014**, *83*, 27.
(80) Pugh, S. F. XCII. Relations between the elastic moduli and the plastic properties of polycrystalline pure metals. *Philos. Mag.* **1954**, *45*, 823.
(81) Lv, H. Y.; Lu, W. J.; Shao, D. F.; Sun, Y. P. Enhanced Thermoelectric Performance of Phosphorene by Strain-Induced Band convergence. *Phys. Rev. B: Condens. Matter Mater. Phys.* **2014**, *90*, 085433.

https://doi.org/10.1021/acsomega.0c06024
ACS Omega 2021, 6, 9433−9441

(82) Ibragimov, K. I.; Korol'kov, V. A. Temperature Dependence of the Work Function of Metals and Binary Alloys. *Inorg. Mater.* **2001**, *37*, 567.
(83) Holzl, J.; Schulte, F. K. Work function of metals. *Springer Tracts in Modern Physics*; Springer, 1979; Vol. *85*.

https://doi.org/10.1021/acsomega.0c06024
ACS Omega 2021, 6, 9433−9441